Pergamon

Int. J. Heat Mass Transfer. Vol. 38, No. 12, pp. 2317–2327, 1995

0017-9310/95 $9.50+0.00

0017-9310(94)00261-4

Inertial effects on thermophoretic transport of small particles to walls with streamwise curvature—II. Experiment†

ATHANASIOS G. KONSTANDOPOULOS‡ and DANIEL E. ROSNER§

Yale University, Department of Chemical Engineering, High Temperature Chemical Reaction Engineering Laboratory, New Haven, CT 06520-208286, U.S.A.

(*Received* 6 *January* 1992 *and in final form* 2 *August* 1994)

Abstract—Directing a high-speed, high-temperature, seeded jet generated by a micro-combustor past the concave side of a 'cold', platinum circular foil whose temperature is actively controlled, we investigate the simultaneous action of inertial and thermophoretic effects on particle deposition from curved, laminar boundary layer flows. Although particle Stokes numbers in these experiments are of $\mathcal{O}(10^{-2})$, much smaller than the values customarily thought to signal the onset of inertial effects, we observe a significant increase of particle deposition rates over those expected based on 'pure thermophoresis' theory, in agreement with a recently developed theory of inertially modified thermophoresis in such flows.

1. INTRODUCTION

The need for rational predictions of *mass* transfer rates from flowing aerosols across non-isothermal boundary layers, arises in many engineering areas such as fouling of power generation equipment (e.g. heat exchanger surfaces, combustion turbine blades, etc.), hot gas clean-up technology (e.g. filtration) and novel materials synthesis in aerosol reactors (e.g. optical waveguides, ceramics, thin films). Frequently, a large part of the particle size spectrum encountered in these high temperature aerosols is in the range where *thermophoresis* and *inertial* transport are expected to be the dominant mass transfer mechanisms. In a previous article [1], herafter referred to as I, we examined theoretically the simultaneous action of inertia and thermophoresis in laminar boundary layer flows along curved walls, in the low Stokes number (ratio of particle relaxation time to a characteristic time scale of the flow), *Stk* limit. One appreciates easily that as *Stk* increases, inertia quickly dominates any other transport mechanism, so the coupling of these two mechanisms is interesting precisely in the limit of weak particle inertia ($Stk \ll 1$). In the present paper we describe an experimental test of the low *Stk*, boundary layer (BL) deposition rate theory described in I, and report for the first time data on inertially augmented thermophoretic deposition rates of inorganic sub-μm particles (MgO) from a high temperature (*ca* 1500 K), atmospheric pressure, BL flow, to cooled, *concave* solid surfaces. The concave shape was chosen for experimental convenience and can be thought of as simulating geometrically the *pressure* surface of a gas turbine blade. As discussed in Section 4, our deposition rate data show that the streamwise curvature induced inertial particle drift, can lead up to a five-fold rate increase over 'pure' thermophoretic deposition, to targets cooled *ca* 30% below the mainstream gas temperature, even for very small (usually considered 'inertialess') particles. This means that systematic corrections will have to be made to the customary practice of predicting deposition behavior of low *Stk* particles from curved non-isothermal BL flows, based only on 'pure' thermophoresis theory, employing the theoretical framework presented in I.

The structure of the present paper is as follows: in Section 2 we describe our experimental set-up, including particle generation, flow–temperature characterization and deposition rate measurement techniques. Section 3 contains the deposition rate measurements and comparisons with theoretical predictions made using the theory of I. In Section 4 we discuss the present results and their implications, summarizing our principal conclusions in Section 5.

2. EXPERIMENTAL

Micro-Jet combustor. Our particle deposition rate experiments are built around a slightly pressurized (*ca* 1.1 atm) micro-combustor (Fig. 1) that provides a steady, high speed–temperature jet, seeded with inorganic MgO particles (see below). This combustor evolved from a previous design used for studies of condensible vapor-assisted supermicron particle

†Based on Ph.D. Dissertation of A. G. Konstandopoulos (Yale University, Engineering and Applied Science).

‡Present address: MicroPhenomena Science & Technology Consulting, 45 Tselepi Str., Thessaloniki, GR-54352, Greece.

§Author to whom correspondence should be addressed.

NOMENCLATURE

d_p	particle diameter
$f''(0)$	0.332
K	particle thermophoretic coefficient
I	reflected laser light intensity
Nu_h	heat transfer Nusselt number
P	pressure
Pr	Prandtl number
R	deposition surface radius of curvature
Re_x	Reynolds number (based on x length)
St_m	mass transfer Stanton number
Stk	Stokes number, $\tau U_\infty/R$
t	time
T	temperature
U_j	jet velocity
x	streamwise body-fitted coordinate
y	normal body-fitted coordinate.

Greek symbols

δ_{BL}	boundary layer thickness
ρ	fluid density
$\tilde{\rho}_p$	intrinsic particle density
τ	particle relaxation time
ω_p	particle mass fraction.

Subscripts

0	initial
e	at the edge of boundary layer
g	gas
p	particle
x	at x location
w	at the wall.

Other

BL	boundary layer (L laminar)
fct( )	function of argument indicated in ( ).

impaction in this laboratory [2] and its availability permitted a convenient extension of those studies into the domain of inertially modified, sub-μm particle thermophoretic transport.

The 110 cm^3 combustion chamber is made of castable ceramic (Ceramcast 528, Aremco Products, Ossining, NY) and includes a spark ignited pilot-burner section. The pilot-burner allows for preheating of the ceramic parts (to avoid thermal shock failures) and provides an ignition source for the main burner. A port is also provided for the introduction of test aerosols. Propane and air (Matheson Gas Products, East Rutherford, NJ) are metered through calibrated flowmeters (Omega, Stamford, CT) and introduced via a co-flow arrangement at the bottom of the main combustion chamber. They mix and ignite with the

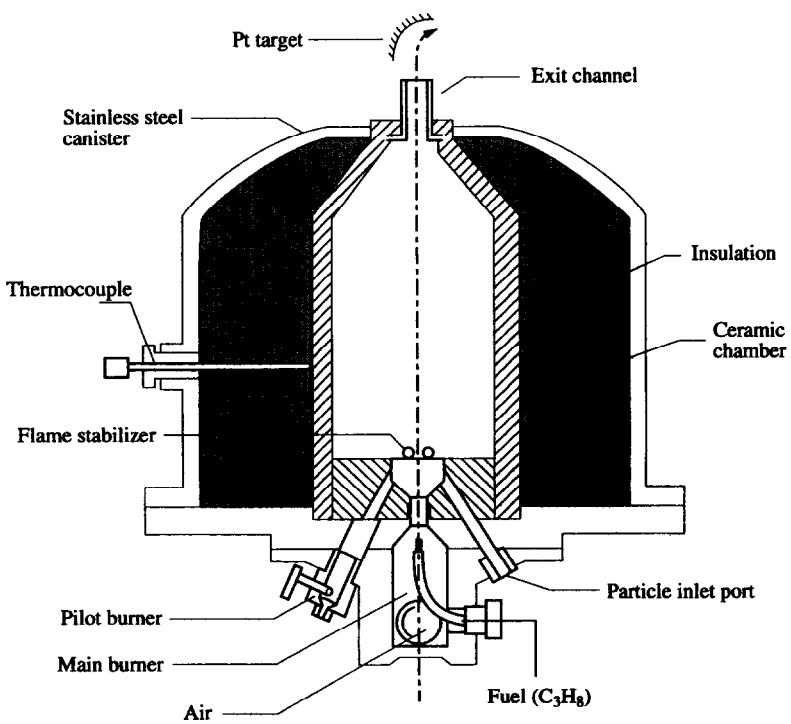

Fig. 1. Cross-sectional view of the microjet burner.

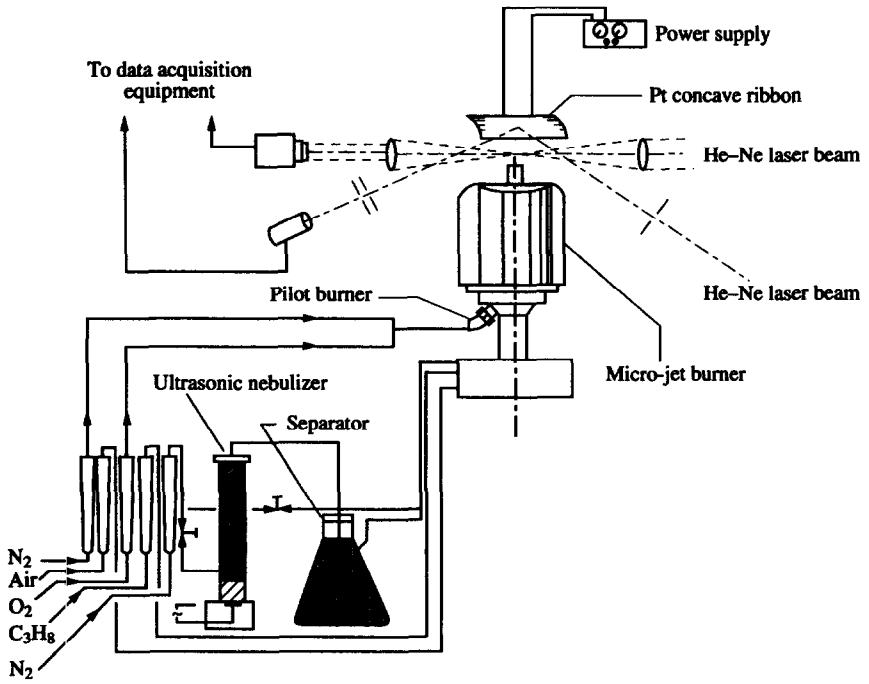

Fig. 2. Schematic of experimental set-up.

aid of the above mentioned pilot-burner in a small pre-chamber, and a flame is stabilized on two ceramic rods (0.5 mm diameter) placed perpendicular to the flow direction at the exit of the pre-chamber. The combustion gases are accelerated via a conical smooth transition at the top of the combustor and finally exit through a square (5×5 mm^2) cross-section platinum duct, embedded in the ceramic cast. The combustion chamber is surrounded by a 50 mm thick ceramic blanket insulation (Cotronics, Brooklyn, NY) which is, in turn, enclosed in a stainless-steel canister. The entire assembly sits on a mechanical base that allows three dimensional spatial motion and rotation around the vertical axis of the combustor, for fine tuning of its position. A 250 μm bead-size platinum/platinum–rhodium (R-type) thermocouple senses the temperature of the outer surface of the ceramic wall and serves as an indicator of steady state operation.

Deposition target. A schematic of our experimental set-up appears in Fig. 2. The combustion aerosol jet is directed parallel to the concave surface of a circular arc deposition target made from platinum foil (6 mm radius, 10 mm arclength, 25 mm long, 0.127 mm thick). The target is held in place by two copper electrodes connected to a Teflon-insulated, aluminum base which is supported by a three-degrees-of-freedom adjustable post for controlled target positioning. The target temperature can be actively controlled either by connecting the supporting electrodes to a 100 A (maximum) power supply (KEPCO, Flushing, NY) or by air-cooling of the rear side of the target using an arrangement of very small nitrogen jets delivered by a perforated 3 mm stainless steel tube, bent parallel to the rear side of the deposition surface and held at a 3 mm distance from it. The target temperature is monitored either with a fine (100 μm bead size) R-type thermocouple, soldered behind the deposition location on the rear surface of the platinum foil, or by a calibrated optical pyrometer (Pyrometer Instrument Co., Bergenfield, NJ). Temperature variations observed with the optical pyrometer along the streamwise direction of the target were found to be at most 5%, when no active temperature control was employed, and below detection limits in the presence of temperature control, hence the deposition surface could be assumed to be isothermal for all experiments reported here. The combination of jet velocities, U_j, possible with our arrangement (maximum velocity attainable is around 140 m s^{-1}) and wall radius of curvature used, R (6 mm) supplies a centrifugal acceleration *ca* 10^4–$10^5 \times g$, that drives the almost 'inertialess' particles, [based on their $\mathcal{O}(10^{-2})$ Stokes number, where Stk ($\equiv \tau U_j/R$) towards the wall and thus modifies the dominant thermophoretic deposition mechanism. Note that the present definition of Stk originates in the theoretical analysis of I and although of the same order of magnitude, it is different from the Stokes number based on the present jet dimensions. A jet-dimension based Stk_{jet} does not incorporate the appropriate flow characteristic time past a curved surface, R/U_j and consequently it is irrelevant for the present problem. Stk_{jet} is of relevance in stagnation point flows against flat surfaces, where it determines the radial extent of particle motion.

Particle generation. A version of the Denton and Swartz [3] ultrasonic nebulizer, available in-house,

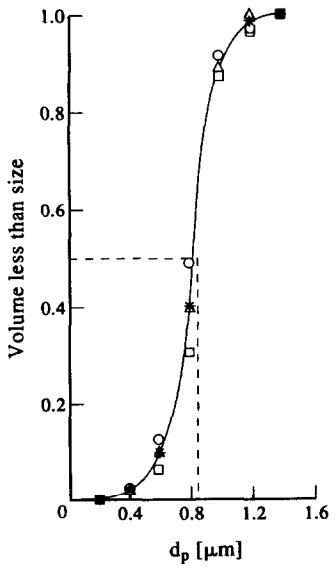

Fig. 3. Size distribution of MgO particles. The symbols refer to different collected samples. The particles have a volume mean diameter of 0.84 μm and a σ_g of 1.2.

was used to disperse an aqueous 0.1 M solution of ultra-pure magnesium-sulfate, $MgSO_4$(s) in a 2 l min^{-1} carrier stream of nitrogen. The aerosol stream passes through a sequence of plenum chambers (that separate out the larger droplets and damp any feed rate unsteadiness) and then is introduced, partially dried, in the combustor through a 120 cm long, 6 mm diameter, flexible hose. The nebulizer set-up includes an air-cooling arrangement to avoid overheating of the piezoelectric transducer (driven at 1350 MHz) that causes the liquid atomization and an inclined, graduated, side glass-tube connected to the solution reservoir, that indicates the amount of remaining solution. A copper–constantan (T-type) thermocouple monitors the solution temperature.

During their residence time (*ca* 30–130 ms, depending on the flow rate) in the combustion chamber the dissolved $MgSO_4$ solution droplets transform rapidly into small, spherical, MgO particles with a 0.84 μm volume mean diameter and a 1.2 standard geometric deviation, σ_g (Fig. 3) as determined by size-insensitive [4] 'pure' thermophoretic sampling and subsequent Scanning Electron Microscopy (SEM). To the extent that all droplets entering the combustor have the same concentration of $MgSO_4$ and experience approximately the same (plug-) flow and temperature history during their transformation, we expect the polydispersity of the MgO solid particle distribution to be approximately the same as that of the solution droplet aerosol. Ultrasonically generated aerosols are typically known to be more polydisperse than the present one, with $\sigma_g \approx 1.5$ [5]. However, this value of σ_g refers to the direct output of the nebulizer, before any conditioning. In the present set-up, the ultrasonically generated aerosol size distribution undergoes several changes as it passes through the delivery system being depleted of the larger particles aerodynamically into the sequence of plenum chambers and of the smaller particles diffusionally in the carrier line. These processes produce an aerosol with a smaller σ_g than the presumably higher, initial σ_g (≈ 1.5). Studies that have addressed the morphology of particles generated upon drying of solution droplets [6, 7] indicate that the resulting solid particles may be porous, their final state being a function of 'process' conditions (relative humidity of carrier gas, solution strength, temperature, etc.). While our particles are in addition subjected to the hot combustor environment, they are nevertheless expected to retain their structure, since the maximum adiabatic flame temperature attained in the combustor is about 2300 K, substantially lower than the MgO(s) melting point (3100 K). In fact, based on the theoretical predictions of I, and as discussed later in Section 3, the particles we generate are likely to be porous with a void fraction around 36%.

A single particle counter based on the principles outlined in ref. [8] was constructed in order to monitor the particle feed-rate *in situ* (see Fig. 2). However, due to sensitivity problems with the available optical detection equipment, we were not able to monitor the sub-μm particle feed rate in the *hot* jet. Instead, we monitored the supermicron solution droplets feed rate under equivalent cold-flow conditions and established that their relative concentration profile across the jet was acceptably uniform (Fig. 4). The concentration of the resulting smaller solid MgO particles in the hot jet is expected to be likewise uniform, considering their much smaller than unity Stokes number (based on exit channel length), their $\mathcal{O}(10^5)$ Schmidt number and jet exit velocity profile (Fig. 4).

The absolute feed rate of the nebulizer was determined with a gravimetric technique passing the aerosol stream before its introduction into the burner through a small (50 cm^3) polyethylene sampling capsule filled with silica-gel and monitoring its rate of weight gain. Employing two capsules in series we confirmed that no measurable quantity of water escaped the first capsule during sampling. Preliminary experiments were conducted to find how long it would take for the particular nebulizer to reach steady-state aerosol production (typically less than 30 min) and subsequently all experiments were conducted after at least a 30 min period of nebulizer warm-up. In all runs, the nebulizer solution feed rate was maintained at 0.037 g min^{-1} and consequently based on solution strength, the particle feed rate was 0.149 mg min^{-1}. Based on geometric optics calculations for the probe volume of the SPC, absolute droplet and particle number count rates were computed to be 2.17×10^8 s^{-1}. These nebulizer solution feed and count rates are consistent with a mass averaged droplet size of 6.9 μm (cf. [5]). Particle number densities depend on the jet flow rate and varied from 1.38 to 2.75×10^{11} m^{-3}. Consequently, interparticle interactions can be neglected and since the MgO mass fraction of the com-

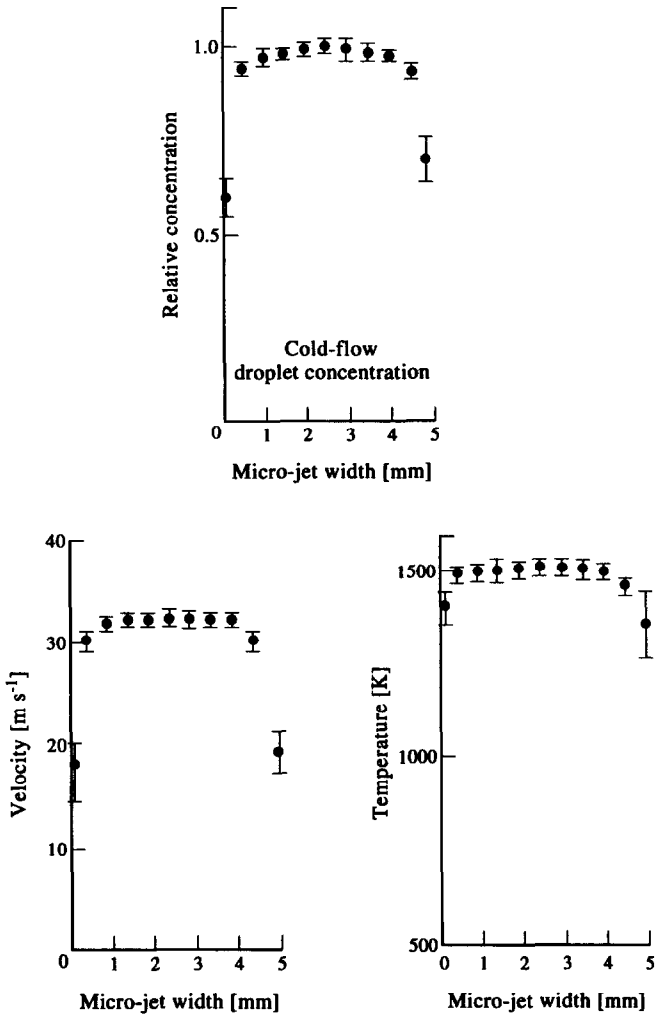

Fig. 4. Jet characterization: hot-flow velocity and temperature profiles and equivalent, cold-flow, droplet concentration profile.

bustor aerosol effluent was negligible, we can also assume that the 'host' gas flow was undisturbed by the presence of the particles.

Deposition rate measurement technique. We have used the real-time laser reflectivity technique of Rosner and Kim [9] to measure *local* initial particle deposition rates at a point on the target located at 0.5 rad turning angle from the leading edge, measured with the aid of a cathetometer. The technique is based on monitoring the decay of the intensity, $I\{t\}$, of a specularly reflected laser beam (here He–Ne) from its 'clean' surface value I_0, as the surface is being covered by depositing particles. Not surprisingly, the initial rate of light intensity decay $-\mathrm{d}(I/I_0)/\mathrm{d}t$ is constant (i.e. $I\{t\}$ is initially linear in t) and is proportional to the rate of change of surface coverage, as found in [9] and also confirmed in the present study, by post mortem SEM calibrations. It is then possible to convert the initial rate of loss of reflectivity into a particle volumetric deposition rate. The laser beam angle of incidence was maintained constant by careful positioning of the target in all experiments. Our best estimate of it is *ca* 50° relative to the normal at the deposition measuring point. Figure 2 shows a schematic of the present optical arrangement, while the reader is referred to [9] for further details on the implementation of these techniques.

Flow and heat transfer characterization. We have experimentally characterized the particle-free flow over the circular concave deposition surface, using specially constructed and instrumented targets geometrically similar to the concave platinum ribbons used for the MgO particle deposition experiments. For the flow measurements we used stainless steel sharp-edge targets, with manometer pressure taps along the flow direction. Streamwise pressure differences from atmospheric pressure were recorded with the help of an inclined tube oil manometer. Free stream (jet) velocities were estimated using a small, ceramic pitot tube (0.3 mm tip diameter with $< 10\%$

low-Re correction), while gas temperatures were measured with fine-wire (50 μm) R-type thermocouples, compensated for radiative/convective heat losses. A typical jet exit velocity and temperature profile is shown in Fig. 4. The velocity measurements when integrated over the jet area were found to be within 5% of the mean velocity determined from total flow rate and jet exit area. This served as a consistency check of our measurement technique. While BL flows over concave surfaces are known to become unstable due to the appearence of Taylor–Görtler vortices [10], in the present experiments we maintained flow conditions well below the experimentally determined instability threshold as given in [10]. This was confirmed by the heat transfer measurements described below, which serve as a sensitive indicator of deviations of the flow from the stable laminar regime. For the heat transfer measurements we used heat insulating concave wedge-shaped, sharp-edge targets constructed from machinable alumina ceramic (Cotronics, Brooklyn, NY), fitted with miniature calorimeters. The transient micro-calorimeter consisted of a high purity copper rod (1.2 mm diameter × 3 mm long) mounted flush with the exposed surface to the flow, with an embedded R-type thermocouple with its leads accessible from the rear of the target. The wedge shape of the target prevented the flow from reaching the rear of the calorimeter which would have affected the measurements. Care was taken to minimize the contact area between the copper block and the ceramic target in order to approximate an adiabatic calorimeter. Using the calorimeter's mass, exposed area, heat capacity and initial slope of transient response, the local wall heat flux could be readily computed (see e.g. [11]).

Heat fluxes measured with the transient calorimeter were converted to a heat transfer Nusselt number, Nu_h and plotted as a function of the local Reynolds number Re_x as shown in Fig. 5(a). The solid line is the classical Polhausen laminar boundary layer (LBL) solution for zero streamwise pressure gradient (flat plate) and constant wall temperature [10]

$$Nu_h = 0.332 Pr^{1/3} \cdot Re_x^{1/2}. \quad (1)$$

The excellent agreement between the measurements and the LBL solution can be further understood examining the pressure distribution measurements. Figure 5(b) depicts the pressure variation along the wall $\Delta P_w\{x\} \equiv P_w\{x\} - P_{atm}$, normalized by the inviscid pressure scale $\rho_g U_j^2/2$ for different jet velocities and parameterized by the global Reynolds number, $Re_R \equiv U_j R/\nu$. $\Delta P_w\{x\}$ is constant up to a turning angle of 1 rad and then starts to decrease as the tail of the wall is reached. The dependence of the dimensionless wall pressure on Re_R is a consequence of the wall curvature. For curved boundary layer flows, pressure differences across the boundary layer scale with δ_{BL}/R [12], as seen from the following scaling analysis of the momentum balance BL equation in the normal direction to the wall:

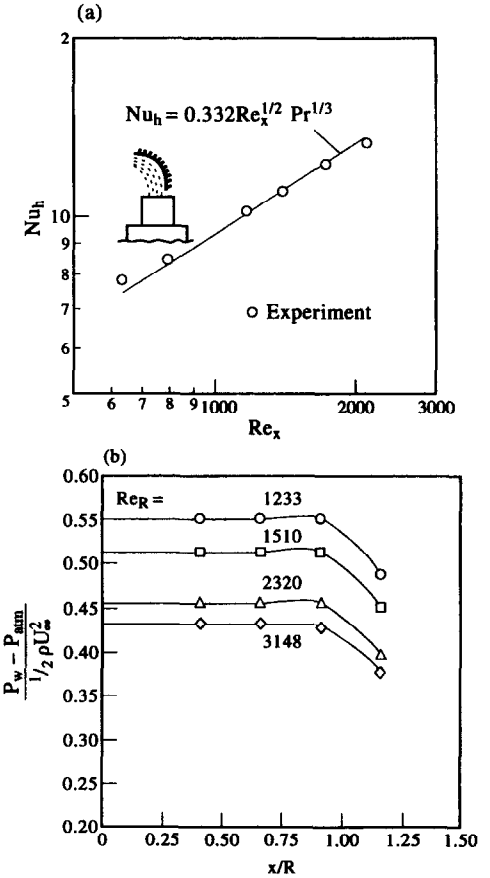

Fig. 5. Flow and heat transfer characterization. (a) Heat transfer Nusselt number, Nu_h, vs Re_x measurements for concave targets. The line is the classic prediction for zero pressure gradient, laminar boundary layer flow. (b) Normalized pressure distribution on a concave target for various Re_R-values.

$$\frac{\partial P}{\partial y} = \rho \frac{u^2}{R} \Rightarrow$$

$$\frac{P_e\{x\} - P_w\{x\}}{\frac{1}{2}\rho U_j^2} \sim \frac{2\delta_{BL}}{R}$$

$$= 2\,\text{const.} \left(\frac{x}{R}\right)^{-1/2} Re_R^{-1/2} \quad (2)$$

so the dimensionless pressure gradient along the outer edge of the LBL, $d\hat{P}_e/dx$ is related to the dimensionless pressure gradient along the wall $d\hat{P}_w/dx$ by:

$$\frac{d\hat{P}_e}{dx} \sim \frac{d\hat{P}_w}{dx} + \text{const.}\, Re_R^{-1/2} \cdot \left(\frac{x}{R}\right)^{-1/2}. \quad (3)$$

The second term on the RHS is small enough for sufficiently high Re_R and therefore dP_w/dx can be used instead of dP_e/dx in the steady Bernoulli equation:

$$\frac{dP_e}{dx} = \rho U_e \frac{dU_e}{dx} \quad (4)$$

to infer the velocity distribution $U_e\{x\}$ along the

outer edge of the LBL. The wall pressure variation of Fig. 5(b) then implies that the flow velocity at the edge of the LBL is constant for up to 1 rad turning angle irrespective of Re_R and then increases slightly towards the trailing edge.

Our heat flux and particle deposition rate measurements were conducted at 0.5 rad turning angle so they were essentially conducted in an effectively zero pressure gradient LBL flow, and the wall curvature has no first-order dynamic effect on either the flow or the heat transfer under the present experimental conditions (cf. ref. [12]). However, the same is far from being true for particle mass transfer. The streamwise wall curvature on BL mass transfer cannot be neglected (cf. I) even for very small particles (conventionally considered inertialess, on the basis of the smallness of their *Stk*). These flow and heat transfer characterization results, valid in the limit of very low particle mass loading, justify our treatment of the flow and temperature fields in our theoretical analysis presented in I.

Experimental procedures. For a typical experiment, we ignite the pilot-burner and slowly preheat the combustor for about an hour until its outer wall temperature stabilizes. At this point the main burner fuel and oxidizer flowmeters are turned on at a preset operating point with the aid of turn-on/shut-off valves and the combustor is left to stabilize again. In addition, the power to the ultrasonic nebulizer transducer is turned on to initiate solution atomization. The nebulizer carrier nitrogen stream is fed into the combustor by-passing the nebulizer via a three-way valve to allow for precise setting of the jet operating conditions. After the warm-up interval of the nebulizer the carrier stream is diverted through the nebulizer and the aerosol is admitted in the combustor. At the same time we monitor the jet temperature and velocity and make any fine adjustments in the combustor flow rates, if necessary, to obtain the desired jet velocity–temperature. Once the jet conditions have been set, we again by-pass the nebulizer and start the target conditioning routine. The platinum foils used were already polished clean with aqua regia, rinsed with distilled water in an ultrasonic bath and mounted on the target holder. The target holder is brought into position, the target exposed to the flow and left to reach the desired temperature (employing the active temperature control system described earlier). At the same time the deposition monitoring laser beam reflects off the target and is collected specularly after spatial and spectral (6333 Å) filtering on a photodiode (EG&G, Princeton, NJ) as shown in Fig. 2. We change abruptly the target temperature a few times in order to relieve any mechanical stress left during mounting that may affect the direction of the specularly reflected light beam, while monitoring its intensity. Once it reaches a constant value, meaning that the system has equilibrated, we let the target temperature stabilize (typically in a few seconds) and then admit abruptly the aerosol into the combustor to start a deposition experiment. The target exposure typically lasts less than 5 min, during which the intensity of reflected light decays linearly, in proportion to the deposition rate, as previously discussed. For each experiment we can then correlate deposition rates with measured deposition conditions. Experimental results were obtained maintaining the gas temperature T_g at 1461 K ($\pm 5.5\%$) and varying wall temperature, T_w, keeping the ratio T_w/T_g in the range 0.7–0.98 while setting jet velocities to 31.5 m s^{-1} ($\pm 3.4\%$) and 72 m s^{-1} ($\pm 5.1\%$).

3. RESULTS

3.1. *Reflectivity curves*

As mentioned, the outcome of each deposition experiment is a time record of normalized reflected light intensity $I(t)/I_0$ ('reflectivity curve'), the initial slope of which, when calibrated against post mortem SEM analysis, gives the local particle volume deposition rate. Figure 6(a) shows a typical reflectivity curve obtained at a temperature contrast ratio (T_w/T_g) of 0.8 and a jet velocity of 31.5 m s^{-1}. This and similar curves show an initial linear part whose slope increases with T_w/T_g consistently with the action of thermophoresis. However, as time passes the surface coverage becomes appreciable and the curves become non-linear, eventually 'saturating' when the deposit surface has reached an 'optically' steady-state structure, and consequently, its reflectivity does not change further. Although not pursued further in the present study, it is of interest to note that the steady-state reflectivity behavior in principle contains information on the deposit surface morphology and its study in the future may provide useful feedback to recent computer simulations of deposit growth from this laboratory [13, 14].

Figure 6(b) shows reflectivity curves obtained with two different jet velocities (31.5 and 72 m s^{-1}) at a fixed T_w/T_g (0.8). The rate of loss of reflectivity is faster for the higher velocity implying a higher deposition rate. Increasing the jet velocity affects deposition rates in two ways. Firstly, by reducing the BL thickness it enhances the temperature gradient and thus increases the strength of thermophoretic deposition. An additional effect comes from the increased particle inertia due to the fact that *Stk* is proportional to the jet velocity. In the present experimental arrangement, we can separate these effects by keeping the jet velocity constant so that the strength of thermophoresis is also constant, and change the radius of curvature of the target to affect the particle *Stk* and thus its inertia. Figure 6(c) shows reflectivity curves obtained at a fixed T_w/T_g (0.8) and jet velocity (31.5 m s^{-1}) and using two different deposition surfaces: a flat target ($R = \infty$) and a concave ($R = 6$ mm) target. It is instructive to compute the particle *Stk*-value in these experiments:

$$Stk \equiv \frac{\tau U_j}{R} = \frac{\tilde{\rho}_p d_p^2}{18\mu} \frac{U_j}{R} C. \quad (5)$$

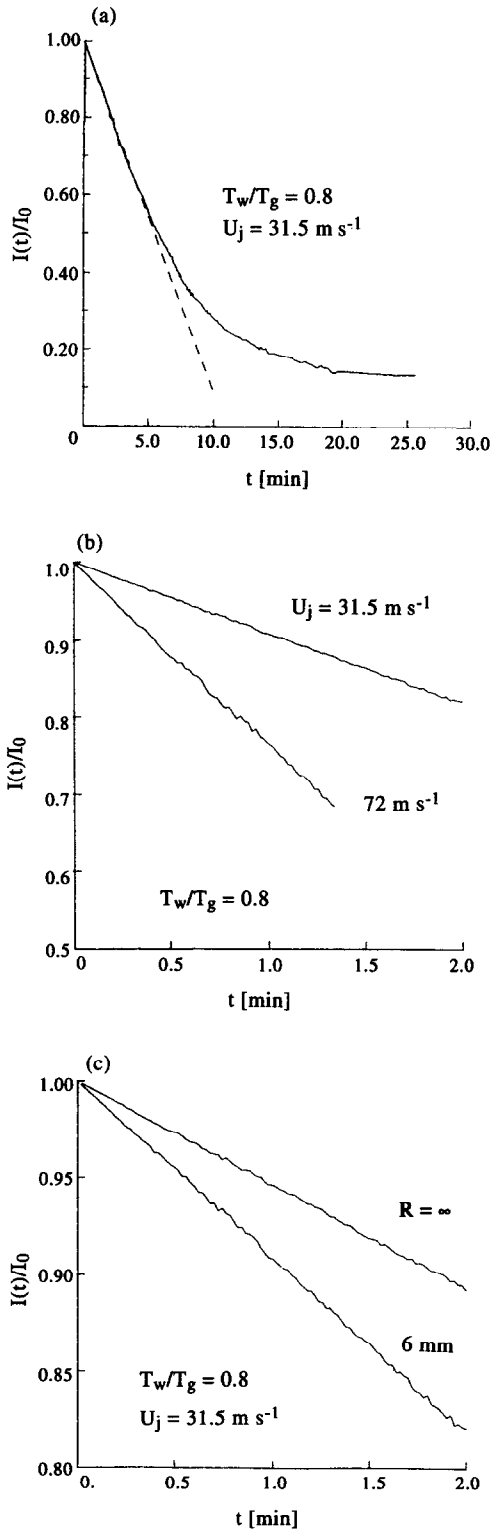

Fig. 6. Reflectivity curves. (a) Intensity of specularly reflected laser beam from Pt target as particle deposition occurs. The reflectivity method of [9] employs the initial slope to infer the deposition rate. (b) Influence of jet velocity on reflectivity curves for thermophoretic deposition. (c) Influence of target surface curvature on reflectivity curves for thermophoretic deposition.

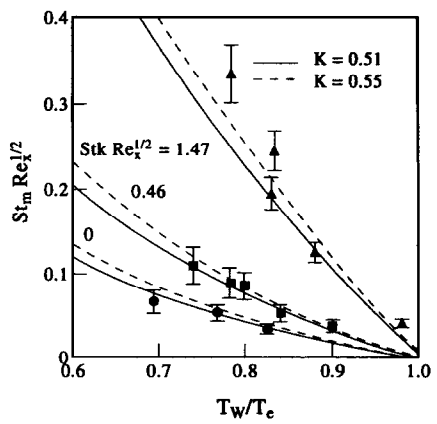

Fig. 7. Comparison of theory and experiments for inertially enhanced thermophoretic deposition to a concave ribbon. The solid lines correspond to a thermophoretic coefficient $K = 0.51$ and the dashed to its free-molecular limit $K = 0.55$.

The Cunningham correction factor C accounts for slip (and ultimately free-molecular) deviations from the continuum Stokes drag form. All variables appearing in equation (5) are known or measurable, except the intrinsic particle density, $\tilde{\rho}_p$. Crystalline MgO has a density of 3.58 g cm^{-3}, however, as mentioned previously, particles generated by drying solution droplets tend to be porous and have a lower density. Thus only an upper bound to Stk can be obtained using the crystalline MgO density. The corresponding maximum Stks for the two curves shown in Fig. 6(c) are then 0 and 0.03, for the flat and the concave target respectively. Interestingly enough, this value of 0.03 is at least an order of magnitude lower than the critical value of Stk where inertial impaction is usually expected to set in, [of $\mathcal{O}(10^{-1})$ for potential flows and $\mathcal{O}(1)$ for creeping flows around spherical and cylindrical collectors]. Furthermore, as we estimated using an ideal inviscid flow field with circular streamlines for the present geometry (which incidentally does not have a critical Stk) inertial enrichment of the particle concentration outside of the BL, does not become appreciable unless $Stk > 0.1$. To interpret such experiments it is necessary to use the theory presented in I for the simultaneous action of thermophoretic and low-Stk inertial effects in curved BL flows.

3.2. *Deposition rate measurements*

As shown in I, the deposition rate of non-Brownian ($Sc \gg 1$) particles can be expressed in dimensionless form as

$$St_m \cdot Re_x^{1/2} = \left(\frac{\omega_{p,w}}{\omega_{p,e}}\right) \cdot \left(\frac{T_e}{T_w}\right) \cdot \left(\frac{T_e}{T_w} - 1\right) \cdot Kf''(0) Pr^{1/3} \quad (6)$$

with the factor $\omega_{p,w}/\omega_{p,e}$ accounting for the fact that the local particle concentration field is modified from its free stream value due to the combined action of inertia and thermophoresis. We present therefore in Fig. 7 our deposition rate results in the form suggested

by equation (6) i.e. as $St_m \cdot Re_x^{1/2}$ vs T_w/T_e, assuming that the temperature at the edge of the BL, T_e, is equal to T_g. Deviations from a single curve would then be due to inertial effects as quantified by the value of $Stk \cdot Re_x^{1/2}$, the relevant inertial parameter for this problem (cf. I). Superimposed on the same graph are the predictions of the inertially modified thermophoretic theory of I which are seen to capture rather well the experimental data. For these predictions we have used the Talbot *et al.* [15] expression to compute the particle thermophoretic coefficient and plotted the curves for various values of $Stk \cdot Re_x^{1/2}$. As discussed in ref. [13] particle rotation in the BL is not expected to make the applicability of the Talbot *et al.* [15] expression questionable under the present conditions. The solid lines in Fig. 7 correspond to our best estimate of the MgO particles thermophoretic coefficient while the dashed lines correspond to the free-molecular limit of the thermophoretic coefficient. As already mentioned, the experimental *Stk*s are not known precisely due to uncertainties in the density of the MgO particles generated upon drying of the solution droplets. However, agreement of the experimental points with the superimposed theoretical curves is consistent with a particle density of 2.29 g cm^{-3} in the computation of all *Stk* (and St_m) values. This density value amounts to assuming a 36% porosity for the dried MgO particles, and is reasonably close to a rough, yet independent estimate of 40% porosity, based on the mass averaged diameter of 6.9 μm, of the ultrasonically generated droplets, estimated in Section 2 (see also ref. [5]), the solute concentration and the dried particle diameter of 0.84 μm obtained from SEM. While porosity of each particle modifies the particle stopping time by an additional factor that depends on its permeability, it can be shown that for the present case this factor is very close to unity. We thus conclude that the present experimental findings are well accounted for by our theory. From the data presented in Fig. 7 we see that inertial enrichment sets in at $Stk \cdot Re_x^{1/2} \sim \mathcal{O}(10^{-1})$ and can enhance thermophoretic deposition rates by five-fold as $Stk \cdot Re_x^{1/2}$ becomes of $\mathcal{O}(1)$, for a moderate temperature contrast ratio, T_w/T_g, of 0.7.

4. DISCUSSION

In the present work we report for the first time the results of an experimental study of the simultaneous occurrence of inertial and thermophoretic effects, during high temperature BL aerosol deposition over curved surfaces. Using simplified bench-top experiments, we have been able to gain important insights of these coupled phenomena which should prove useful in examining such interactions in more complex geometries (e.g. gas turbine blade cascades).

Our experimental results (Fig. 7) suggest that it is permissible to neglect (curvature induced) inertial effects in BL flows only for say, $Stk \cdot Re_x^{1/2} < \mathcal{O}(10^{-1})$. To appreciate the range of applicability

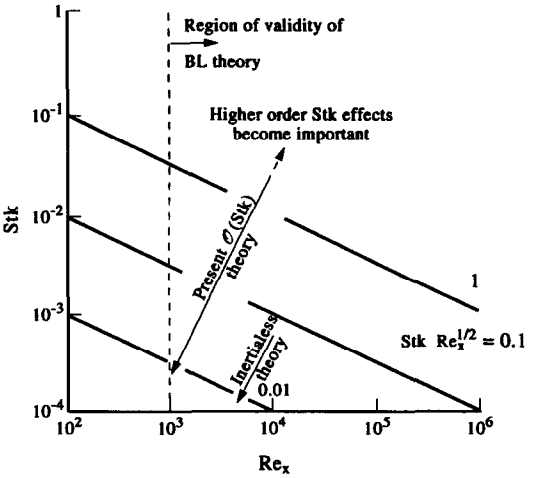

Fig. 8. Inertialess vs present inertial boundary layer deposition theory on the (Stk, Re_x) map.

of the present results and to delineate the limits of validity of the inertialess (pure thermophoretic) analysis for deposition from BL flows over curved surfaces we have constructed the map of Fig. 8 considering the parameter space of interest in say, fossil-fuel power generation environments. As seen in Fig. 8 the inertialess analysis is expected to have a small range of validity since it depends on 'conflicting' requirements for $Stk(\ll 1)$ and $Re_x^{1/2}$ $(\gg 1)$. On the contrary, the inertial theory of I has the advantage that it is asymptotically exact in these limits and as a consequence has a much wider range of applicability.

In terms of particle sizes the following order of magnitude estimate can be made for a high-temperature (*ca* 1200 K) environment:

$$Stk \cdot Re_x^{1/2} = \frac{1}{18} C \frac{\tilde{\rho}_p}{\rho_e} Re_R^{3/2} \cdot \left(\frac{d_p}{R}\right)^2 \cdot \left(\frac{x}{R}\right)^{1/2} < 0.1 \quad (7)$$

which for typical densities of inorganic ash particles and a collector $Re_R \sim \mathcal{O}(10^5)$ gives: $d_p/R < 10^{-6}$. For common radii of curvature $R \sim \mathcal{O}(10^{-2}$ m) our estimate gives $\mathcal{O}(0.01$ μm) as the 'cut-off' diameter above which inertial effects should be included for accurate predictions of deposition rates. Of course the restriction of equation (7) would always be true in a very small region [such that $(x/R)^{-1/4}$ is sufficiently large to make it valid] near the stagnation point of a bluff body, or at the beginning of a bend, or near the leading edge of the Pt-foil used in our experiments (however BL theory is not valid in this latter case). In these cases the inertialess analysis could be used, provided that the assumptions $Stk(\ll 1)$ and $Re_x^{1/2}$ $(\gg 1)$ are still valid. It should be stressed that although the present study considered how inertial effects modify thermophoretic transport, the previous estimates for the onset of inertial effects in curved BLs are expected to be largely independent of the prevailing transport mechanism [13].

An important consequence of the low *Stk*, BL iner-

tial effects considered here and in I, is the breaking of the now-familiar heat-mass transfer 'analogy' encountered in pure thermophoresis [16–18]. The local particle mass fraction over an isothermal boundary, colder than the mainstream, is to a very good approximation uniform. This will be true provided that the particles originate from a region of uniform temperature and concentration. Under these conditions the aforementioned analogy then states that thermophoretic mass transfer rates are proportional to the heat-flux to the boundary and can be estimated from more readily available heat transfer measurements. The value of such a simple scheme is obvious since it permits the extension of many heat flux correlations in complex flow geometries to the domain of thermophoretic mass transfer. The present study shows that systematic generalizations [13] to this scheme will have to be sought when $Stk \cdot Re_x^{1/2}$ is not negligible, in the spirit of the analysis presented in I.

For convenience in this first effort we have studied experimentally deposition to concave surfaces with effectively zero streamwise pressure gradient, colder than the mainstream flow. The study of convex surfaces should present no problem provided that we stay above the lower threshold of the reflectivity detection scheme, since now we would be measuring depletion rather than enrichment of particle deposition rates as the inertial parameter $Stk \cdot Re_x^{1/2}$ is increased. In addition, the study of hot-walls and how particle inertia affects their associated particle-free regions (cf. I) is also possible with the present experimental set-up. The interpretation of such new measurements can be also effected employing the theoretical method of I, at least until the onset of flow separation for the convex case or Taylor–Görtler vortices for the concave case.

The fluid mechanics of the host-flow can be straightforwardly extended from the simple case considered here to other geometries to include non-zero pressure gradients (e.g. using miniature turbine blade models, cylinders in cross-flow, etc.). Similarly, the theory can incorporate such and/or variable property effects, at the expense of numerical complexity. In all cases the crucial parameter governing inertial effects is still the BL (effective) Stokes number $Stk \cdot Re_x^{1/2}$. For complete predictions however, an additional problem has to be solved, namely that of computing the particle concentration at the 'outer' edge of the mass transfer BL (which here coincides with the *heat transfer* BL). This concentration will be systematically enriched or depleted from its free-stream value. Such an inviscid inertial enrichment/depletion (outside the BL) depends only on Stk [19]. Here due to our experimental design, the particle concentration at the outer edge of the BL was expected and confirmed theoretically to be essentially that of the jet.

We have hinted that the upper limit of validity of the present results with respect to Re_x (provided that Stk is small) is dictated by the onset of fluid-dynamic instabilities that will eventually lead to turbulence. Although extensive experimental data exist on inertial effects on particle transport in isothermal, straight, turbulent BLs ('eddy-impaction') there is a scarcity of data on particle transport in turbulent, non-isothermal, curved BLs even for inertialess particles, and the extension of the present experimental and theoretical studies to such cases should be given a high research priority. Other phenomena may also come into play at higher Re_x even before transition to turbulence, such as shear-induced removal of predeposited particles or the inability of a particle to find a 'stable home' in the deposit [20]. In fact, we have observed at higher jet velocities (120 m s^{-1}) than the ones reported here, a decrease in deposition rates. However, we have not yet undertaken a systematic study of such cases. Similar observations were recently reported by Makel and Kennedy [21] in their investigation of pure thermophoretic, organic soot deposition in stagnation point flows. In that study a decrease of net deposition rate set in at 1000 s^{-1} velocity gradient and this was attributed to shear-induced particle removal.

5. CONCLUSIONS

Based on bench-top, high temperature BL particle deposition experiments, using concave targets, and related theoretical calculations [1], we draw the following conclusions for the simultaneous action of thermophoretic and inertial effects:

(1) Observed particle deposition rates are in good agreement with the inertially modified BL transport analysis of I. This comparison confirms the theoretically anticipated, significant effects of particle inertia on deposition rates, even at small enough Stk when customarily (and incorrectly) these effects are assumed to be negligible.

(2) The importance of inertial effects on thermophoretic transport in BL layers with streamwise curvature in the small Stk limit is controlled by $Stk \cdot Re_x^{1/2}$ rather than Stk alone.

(3) Limits of applicability of the commonly used inertialess analysis and relevant criteria were given. For $Stk \cdot Re_x^{1/2}$-values of order 10^{-1} and higher, the inertialess analysis would grossly miscalculate the actual deposition rate. These criteria in conjunction with the present theory of inertially modified thermophoretic transport, are expected to enhance the reliability of mass transfer rate predictions in aerosol deposition to curved surfaces.

In closing we re-affirm the following view of low Stk inertial phenomena emerging from last decade's research in this laboratory: even though particle inertia by itself may not be able to cause the deposition of small Stk particles, it acts co-operatively with any other non-negligible transport mechanism present. As a result, the particle concentration at the deposition surface and thus the particle deposition rate can be affected dramatically.

Acknowledgements—We wish to thank Prof. Y. Goldman (Technion, Israel) for the initial development of the microjet burner. We are also indebted to Profs. A. Gomez and J. Fernández de la Mora (Yale, ME Dept.) for their helpful advice and comments. This work has been supported in part by the U.S. Department of Energy–Pittsburgh Energy Technology Center, under Grants No. DE-FG22-86PC90756 and DE-FG-2-90PC90099, the U.S. Air Force Office of Scientific Research under Grants No. 89-0223 and 91-0170, and the Yale HTCRE Lab Industrial Affiliates: Union Carbide, E. I. DuPont de Nemours and Co., General Electric, Shell and SCM-Chemicals. AGK was the recipient of the Pierre W. Hoge Fellowship (administered by the Yale University Graduate School) during part of this study. A preliminary version of this article was presented orally as Paper 7C.6 at the 1990 Annual Meeting of the American Association for Aerosol Research, 18–22 June, Philadelphia, PA.

REFERENCES

1. A. G. Konstandopoulos and D. E. Rosner, Inertial effects on thermophoretic transport of small particles to walls with streamwise curvature—I. Theory, *Int. J. Heat Mass Transfer* **38,** 2305–2315 (1995).
2. A. G. Konstandopoulos, Y. Goldman and D. E. Rosner, Experimental studies of inorganic particle-laden high temperature–velocity jet impingement at collecting surfaces: Sticking and deposit erosion in the simultaneous presence of condensing alkali sulfate vapors, presented at the 18th Annual Meeting of the Fine Particle Society, Symposium on Multiphase Flow, Boston, MA, 3–7 August (1987).
3. M. B. Denton and D. B. Swartz, An improved ultrasonic nebulizer system for the generation of high density aerosol dispersions, *Rev. Scient. Instrum.* **45**(1), 81–83 (1974).
4. D. E. Rosner, D. W. Mackowski and P. García-Ybarra, Size and structure insensitivity of the thermophoretic transport of aggregated 'soot' particles in gases, *Comb. Sci. Technol,* **80,** 87–101 (1991). See also: D. E. Rosner *et al., Ind. Engng Chem. Res.* **31,** 760–769 (1992).
5. R. Dennis (Ed.), *Handbook on Aerosols.* available as Publication TID-26608 from U.S. Dept. of Commerce NTIS, Springfield, VA 22161 (1976).
6. K. H. Leong, Morphology of aerosol particles generated from the evaporation of solution drops, *J. Aerosol Sci.* **12**(5), 417–435 (1981).
7. K. H. Leong, Morphological control of particles generated from the evaporation of solution droplets: theoretical considerations, *J. Aerosol Sci.* **18**(5), 511–524 (1987).
8. D. J. Holve, D. Tichenor, J. C. F. Wang and D. R. Hardesty, Design criteria and recent developments of optical single particle counters for fossil fuel systems, *Optical Engng* **20**(4), 529–539 (1981).
9. D. E. Rosner and S. S. Kim, Optical experiments on thermophoretically augmented submicron particle deposition from 'dusty' high temperature gas flows, *Chem. Engng J.* **29,** 147–157 (1984).
10. H. Schlichting, *Boundary Layer Theory.* McGraw-Hill, New York (1955).
11. D. E. Rosner, *Transport Processes in Chemically Reacting Flow Systems,* Butterworths, Stoneham, MA (1986). (Third printing 1990.)
12. L. Rosenhead (Ed.), Laminar Boundary Layers. Oxford University Press, Oxford (1963). Also available as a Dover Paperback.
13. A. G. Konstandopoulos, Effects of particle inertia on aerosol transport and deposit growth dynamics, Ph.D. Dissertation, Yale University, New Haven, Connecticut (1991).
14. M. Tassopoulos, Relationships between particle deposition mechanisms, deposit microstructure and effective transport properties, Ph.D. Dissertation, Yale University, New Haven, Connecticut (1991).
15. L. Talbot, R. K. Cheng, R. W. Schefer and D. R. Willis, Thermophoresis of particles in heated boundary layers, *J. Fluid Mech.* **101**(4), 737–758 (1980).
16. S. L. Goren, Thermophoresis of aerosol particles in the laminar boundary layer on a flat plate, *J. Colloid Interface Sci.* **61**(1), 77–85 (1977).
17. D. E. Rosner and J. Fernández de la Mora, Small particle transport across turbulent nonisothermal boundary layers, *ASME Trans. J. Engng Pwr* **104,** 885–894 (1982).
18. G. K. Batchelor and C. Shen, Thermophoretic deposition of particles in gas flowing over cold surfaces, *J. Colloid Interface Sci.* **107**(1), 21–37 (1985).
19. J. Fernández de la Mora and D. E. Rosner, Inertial deposition of particles revisited and extended: Eulerian approach to a traditionally Lagrangian problem, *Physicochem. Hydrodyn.* **2,** 1–21 (1981).
20. D. E. Rosner, A. G. Konstandopoulos, M. Tassopoulos and D. W. Mackowski, Deposition dynamics of combustion-generated particles: summary of recent studies of particle transport mechanisms, capture rates and resulting deposit microstructure/properties. In *Inorganic Transformations and Ash Deposition During Combustion* (Edited by S. A. Benson), pp. 585–606. Engineering Foundation ASME, New York (1992).
21. D. B. Makel and I. M. Kennedy, Experimental and numerical investigation of soot deposition in laminar stagnation point boundary layers, *Proceeding of the Twenty-Third International Symposium on Combustion,* The Combustion Institute, Pittsburgh, PA, pp. 1551–1557 (1990).